*Article*

# Flexible Carbon Fiber/SnO$_2$@rGO Electrode with Long Cyclability for Lithium-Ion Batteries

Wenjie Zhang [1,*] , Yongqi Liu [1], Zhouyang Qin [2], Lingxiao Yu [2], Jiabiao Lian [1,*], Zhanliang Tao [3] and Zheng-Hong Huang [2,4,*]

[1] Institute for Energy Research, Jiangsu University, Zhenjiang 212013, China
[2] State Key Laboratory of New Ceramics and Fine Processing, School of Materials Science and Engineering, Tsinghua University, Beijing 100084, China
[3] Key Laboratory of Advanced Energy Materials Chemistry (Ministry of Education), Nankai University, Tianjin 300071, China
[4] Key Laboratory of Advanced Materials (MOE), School of Materials Science and Engineering, Tsinghua University, Beijing 100084, China
* Correspondence: zwenjie@ujs.edu.cn or zwenjie1008@hotmail.com (W.Z.); jblian@ujs.edu.cn (J.L.); zhhuang@tsinghua.edu.cn (Z.-H.H.)

**Abstract:** Flexible electrodes are highly desirable for next-generation wearable lithium-ion batteries. To achieve high-capacity flexible electrode materials, SnO$_2$ with high theoretical capacity has been introduced into electrodes and shows promising capacity. However, the electrodes are still confronted with major challenges in terms of inferior rate capability and cycling stability, which are caused by large volume changes of SnO$_2$ during the lithiation/delithiation process. Here, we adopt an adsorption assembly strategy to fabricate a flexible carbon fiber/SnO$_2$@rGO electrode that effectively stabilizes the volume changes of SnO$_2$ and enhances the charge transport kinetics in electrodes. The sandwich-like structure endows the electrode's high flexibility and succeeds in improving both rate capability and cycling stability. The flexible carbon fiber/SnO$_2$@rGO electrode delivers a high capacity of 453 mAh g$^{-1}$ at 50 mA g$^{-1}$ and outstanding capacity retention of 88% after 1000 cycles at 2 A g$^{-1}$.

**Keywords:** lithium-ion batteries; flexible electrode; carbon fiber/SnO$_2$@rGO; adsorption assembly; long cyclability

## 1. Introduction

As demand for wearable lithium-ion batteries (LIBs) escalates, flexible electrodes have excellent prospects for future energy storage materials [1–4]. Compared with conventional powdered electrode materials, flexible electrode materials can be directly assembled into batteries without the need for a current collector, polymeric binder, or conductive additive [5–7]. In addition to its unique flexibility, it is also crucial to achieve the optimized high capacity, rate capability, and cycling stability. High-capacity flexible electrode materials are often prepared by combining flexible conductive substrates with high theoretical capacity materials, such as transition-metal oxides, transition-metal sulphides, MXenes, and silicon-based materials [8–11]. Among them, SnO$_2$ with high theoretical capacity (782 mAh g$^{-1}$) has been introduced into electrodes and shown attractive capacity [12–15]. However, the low conductivity and drastic volume expansion of SnO$_2$ during cycling give rise to electrode pulverization and high charge-transfer resistance, resulting in inferior cyclability and rate capability [16–18].

To achieve desirable electrochemical performance, it is crucial to mitigate the volume expansion of SnO$_2$ and enhance charge transport kinetics. Significant efforts have been made to address these issues through nanoengineering and structural design. Nanoengineering effectively increases electrode-electrolyte contact area and enables fast access for lithium ions, thereby enhancing charge transport kinetics [19–22]. Meanwhile, nanosizing reduces internal stresses during volume change and improves cyclability [20,23].

Consequently, researchers have synthesized $SnO_2$ at the quantum dot scale to improve electrochemical performance [24–26]. Recent studies also demonstrated the importance of structural design in improving electrochemical performance [27–29]. Pre-reserve cavities in $SnO_2$ particles are helpful for the alleviation of the mechanical strain of $SnO_2$ during the lithiation/delithiation process [30]. Therefore, $SnO_2$ with hollow or porous structures has been explored to buffer the volume expansion [31–33]. Deliberate structural design of the entire electrode via hybridizing $SnO_2$ with carbonaceous materials or conductive polymers is also effective for improving conductivity and structural stability [34–36]. Various electrode structures have been designed and constructed, including $SnO_2$@polypyrrole [37], expanded graphite@$SnO_2$@polyaniline [38], lotus-seed-pod-like $SnO_2$@CNF [2], nanosheet-like $SnO_2$@C/expanded graphite [39], cubic hollow $SnO_2$@C [40], dual carbon shells C@$SnO_2$@C [41], bowl-like $SnO_2$@carbon [42], C-$SnO_2$ nanofibers [43], and yolk-shell structured $SnO_2$@void@C porous nanowires [44]. The above findings demonstrate that nanoengineering and structural design can effectively alleviate the volume expansion and enhance the charge transport kinetics in electrodes. However, most of the reported materials either are in the form of powders or require complex fabrication technologies. Electrospinning, hydrothermal synthesis, hard template method, and chemical vapor deposition are widely employed techniques in the nanoengineering and structural design of electrode materials [37,45–47]. However, electrospinning necessitates high voltage and stringent experimental conditions, which can be significantly influenced by solution concentration and environmental factors, including temperature and humidity. Hydrothermal synthesis requires elevated temperature and pressure, limiting its application to certain flexible substrates; for instance, the flexibility of filter paper substrates is compromised during the hydrothermal process. The hard template method typically involves complex synthesis procedures, such as an additional post-processing step for the removal of templates, which hinders scalable production. Chemical vapor deposition necessitates expensive equipment, thereby increasing the overall cost of electrode materials. Therefore, simple fabrication technology is highly demanded in the synthesis of flexible $SnO_2$-based electrodes with desirable electrochemical performances.

In this study, we adopt a simple adsorption assembly strategy to fabricate a flexible carbon fiber/$SnO_2$@rGO electrode, effectively addressing these challenges. The filter paper was sequentially immersed in $SnCl_2$ solution and graphene oxide (GO) solution, followed by carbonization to produce the sandwich-like flexible carbon fiber/$SnO_2$@rGO electrode. The filter paper serves as both the precursor for carbon fiber and the substrate for anchoring guest materials. Its excellent absorbent property facilitates the infiltration of precursor solutions, enabling effective adsorption of $Sn^{2+}$ and GO onto the paper surface during the adsorption assembly process. The sandwich-like configuration, with rGO encapsulating $SnO_2$, mitigates the volume expansion of $SnO_2$ and enhances charge transport kinetics. Consequently, the flexible carbon fiber/$SnO_2$@rGO electrode exhibits high-rate capability and outstanding cycling stability, retaining 88% of its capacity after 1000 cycles at 2 A $g^{-1}$. Additionally, this simple adsorption assembly strategy has the advantage of solving the crucial problem caused by volume change and shows potential for practical applications.

## 2. Materials and Methods

### 2.1. Materials Preparation

The filter paper utilized in this study is the medium-speed qualitative variety (New Star, 102) produced by Hangzhou Special Paper Industry Co., Ltd., Hangzhou, China. Its pore size and thickness are 7–8 μm and 0.15 mm, respectively. This filter paper is made of α-cellulose derived from cotton fibers. The ash content is less than 0.15%. The filter paper was first immersed in 0.03 M $SnCl_2$ (Sinopharm Chemical Reagent Co. Ltd., Shanghai, China) aqueous solution and subsequently dried in an oven at 100 °C. Following this, the dried filter paper was immersed in 2 mg $ml^{-1}$ GO aqueous solution and again dried in the oven at 100 °C. The resulting filter paper was then calcined at 500 °C for 4 h in Ar. After calcination, the flexible

carbon fiber/SnO$_2$@rGO electrode was obtained. The control carbon fiber/SnO$_2$ electrode was obtained under the same conditions without immersion in the GO solution.

### 2.2. Material Characterizations

Crystal structures of the samples were analyzed using X-ray diffraction (XRD, Bruker D8-ADVANCE, Bruker, Karlsruhe, Germany) under an accelerating voltage of 40 kV. Morphologies and elemental energy spectra were characterized by scanning electron microscopy (SEM, Dual-beam FIB 235, FEI Strata, Hillsboro, OR, USA) and transmission electron microscopy (TEM, JEM-2100F, JEOL, Akishima, Tokyo). To evaluate the electrochemical performances, coin-type cells were assembled with the prepared samples as the working electrode, lithium foil as the counter electrode, and 1 M LiPF$_6$ in EC/DMC/EMC (1:1:1 in volume) as the electrolyte. Cyclic voltammetry (CV) and electrochemical impedance spectroscopy (EIS) were performed using an electrochemical workstation (VMP3, Bio-Logic, Knoxville, TN, USA). CV curves were recorded at a scan rate of 0.5 mV s$^{-1}$ over a potential range of 0.01 to 3 V. EIS measurements were conducted with an AC amplitude of 10 mV across a frequency range of 100 kHz to 0.01 Hz. The potentials for the EIS measurements of the carbon fiber/SnO$_2$@rGO electrode and carbon fiber/SnO$_2$ electrode were approximately 2.24 V and 1.72 V, respectively, corresponding to the open circuit potentials of the coin-type cells. Galvanostatic discharge/charge curves were obtained using a Land battery testing system (Jinnuo Electronics Co., Wuhan, China) between 0.01 and 3 V.

### 3. Results and Discussion

Figure 1 illustrates the preparation process of the flexible carbon fiber/SnO$_2$@rGO electrode. Initially, the filter paper was immersed in an aqueous SnCl$_2$ solution, allowing Sn$^{2+}$ cations to adhere to the surface of the filter paper fiber (Figure 1a,b). The soaked filter paper was subsequently dried in an oven at 100 °C. Following this, the filter paper was immersed in a graphene oxide (GO) solution and again dried in the oven at 100 °C (Figure 1c). Finally, the resultant filter paper was calcined to produce the flexible carbon fiber/SnO$_2$@rGO electrode (Figure 1d). During the calcination process, the filter paper fiber, Sn$^{2+}$ ions, and GO were converted into conductive carbon fiber, SnO$_2$, and reduced graphene oxide (rGO), respectively. For comparison, the control carbon fiber/SnO$_2$ electrode was prepared using the same method, omitting the immersion in GO solution (Figure 1a,b,e).
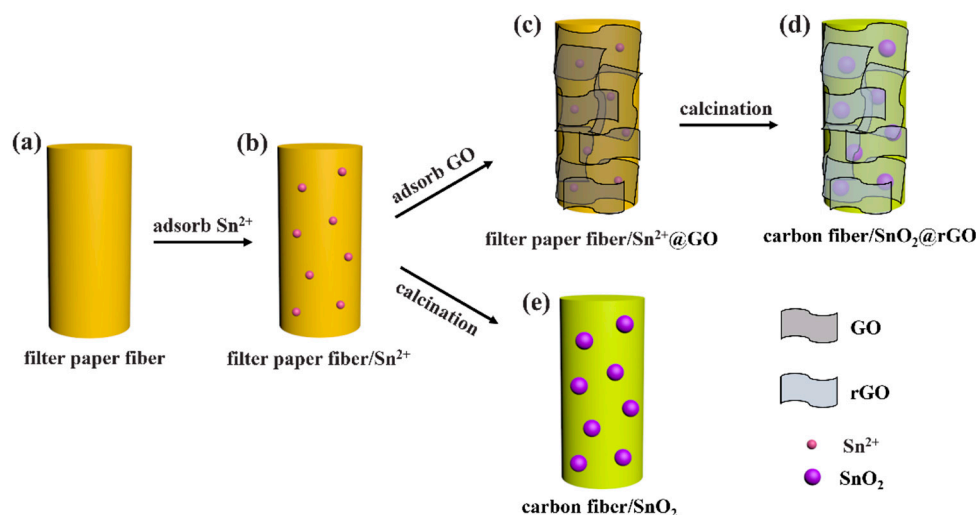


**Figure 1.** Schematic diagram of the preparation process of flexible carbon fiber/SnO$_2$@rGO. (**a**) filter paper. (**b**) Filter paper fiber after being immersed in SnCl$_2$ solution. (**c**) Filter paper fiber/Sn$^{2+}$ after being immersed in GO solution. (**d**) Carbon fiber/SnO$_2$@rGO. (**e**) Carbon fiber/SnO$_2$.

Figure 2 shows the transformation from filter paper to carbon fiber/SnO$_2$@rGO. Filter paper has excellent absorbent ability for easy infiltration of the precursor solution. Fol-

lowing an adsorption process, filter paper transitions from white to dark (Figure 2a,b), and its surface becomes rough due to the adsorption of $Sn^{2+}$ ions and GO onto the filter paper fiber (Figure 2e–i). Morphological and elemental energy spectra analyses indicate that $Sn^{2+}$ and GO have successfully adsorbed onto the filter paper fiber after the adsorption process (Figure 2f,g,i). After carbonization, the resulting filter paper is transformed into a carbon fiber/$SnO_2$@rGO electrode (Figure 2c). The presence of rGO is beneficial to enhance the overall flexibility of the electrode. As shown in Figure 2d, the carbon fiber/$SnO_2$@rGO electrode exhibits excellent flexibility and can be bent without compromising its structural integrity.
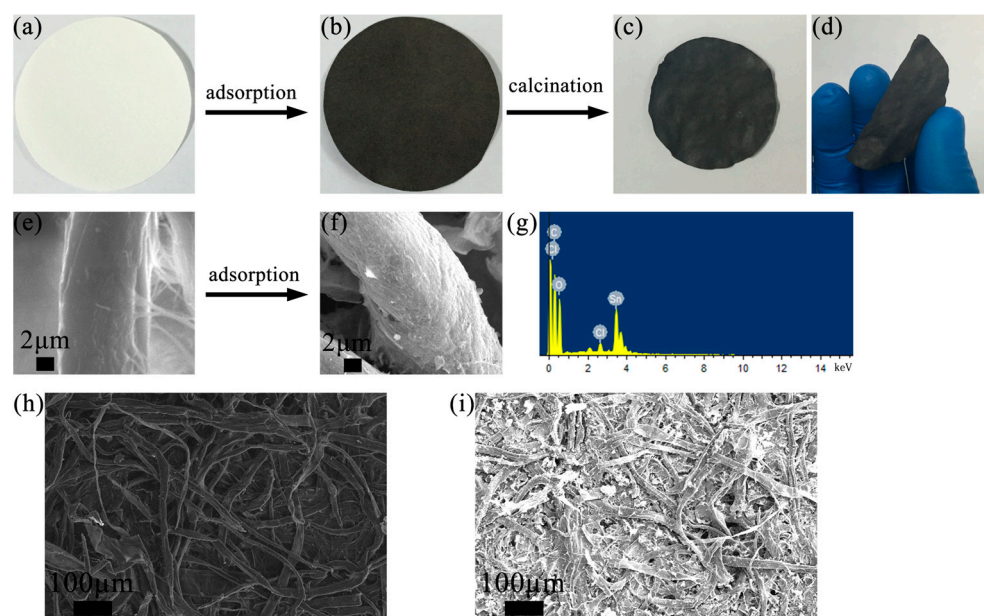


**Figure 2.** Photographs of (**a**) filter paper, (**b**) filter paper after adsorption assembly, and (**c,d**) flexible carbon fiber/$SnO_2$@rGO. (**e,h**) SEM image of filter paper fiber. (**f,i**) SEM image of filter paper fiber after adsorption. (**g**) Elemental energy spectra of filter paper fiber after adsorption.

Figure 3a shows the X-ray diffraction (XRD) pattern of the obtained flexible carbon fiber/$SnO_2$@rGO and carbon fiber/$SnO_2$. For the carbon fiber/$SnO_2$@rGO, the broad peak observed between 16° and 24° is indexed to carbon and rGO [48,49]. For the carbon fiber/$SnO_2$, the broad peak around 16° is related to carbon. The other diffraction peaks correspond to the $SnO_2$ phase (JCPDS No. 41-1445). Figure 3b presents the elemental energy spectra of the carbon fiber/$SnO_2$@rGO. The result indicates that there are no Cl elements present in the carbon fiber/$SnO_2$@rGO, confirming that $Cl^-$ ions were eliminated during the carbonization process at 500 °C.
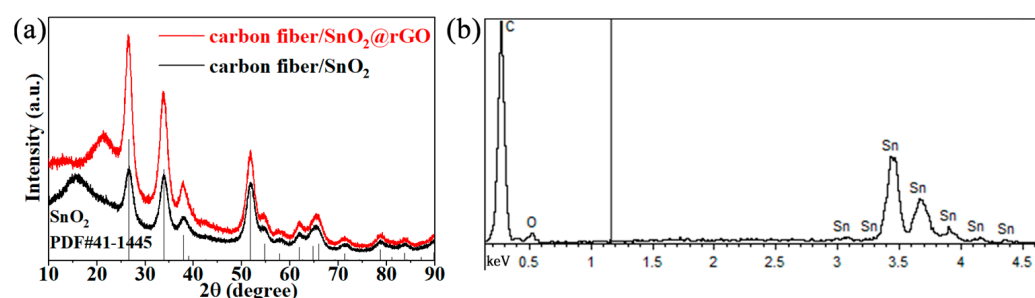


**Figure 3.** (**a**) XRD pattern of flexible carbon fiber/$SnO_2$@rGO and carbon fiber/$SnO_2$. (**b**) Elemental energy spectra of flexible carbon fiber/$SnO_2$@rGO.

Figure 4a shows the morphology of the pure carbon fiber which was obtained by directly carbonizing filter paper without any prior adsorption treatment. SEM shows

that the surface of the carbon fiber is smooth and there are no other substances on the surface. Compared to pure carbon fiber, the low-magnification SEM images of carbon fiber/$SnO_2$@rGO indicate that the outermost layer is entirely covered by rGO (Figure 4b,c). High-magnification SEM further demonstrates that the carbon fiber/$SnO_2$@rGO has a sandwich-like structure (Figure 4d). The $SnO_2$ particles located on the carbon fiber are well coated by rGO. The microstructure was further characterized by HRTEM (Figure 4e). It reveals the well-crystallized $SnO_2$ particles with a lattice fringe of 0.33 nm, which corresponds to the d-spacing of diffraction planes (110) [50]. Additionally, the HRTEM image also confirms the structure of $SnO_2$ encapsulated by rGO, while for the carbon fiber/$SnO_2$, the bare $SnO_2$ particles are located on the surface of the carbon fiber without rGO coating (Figure 4f).
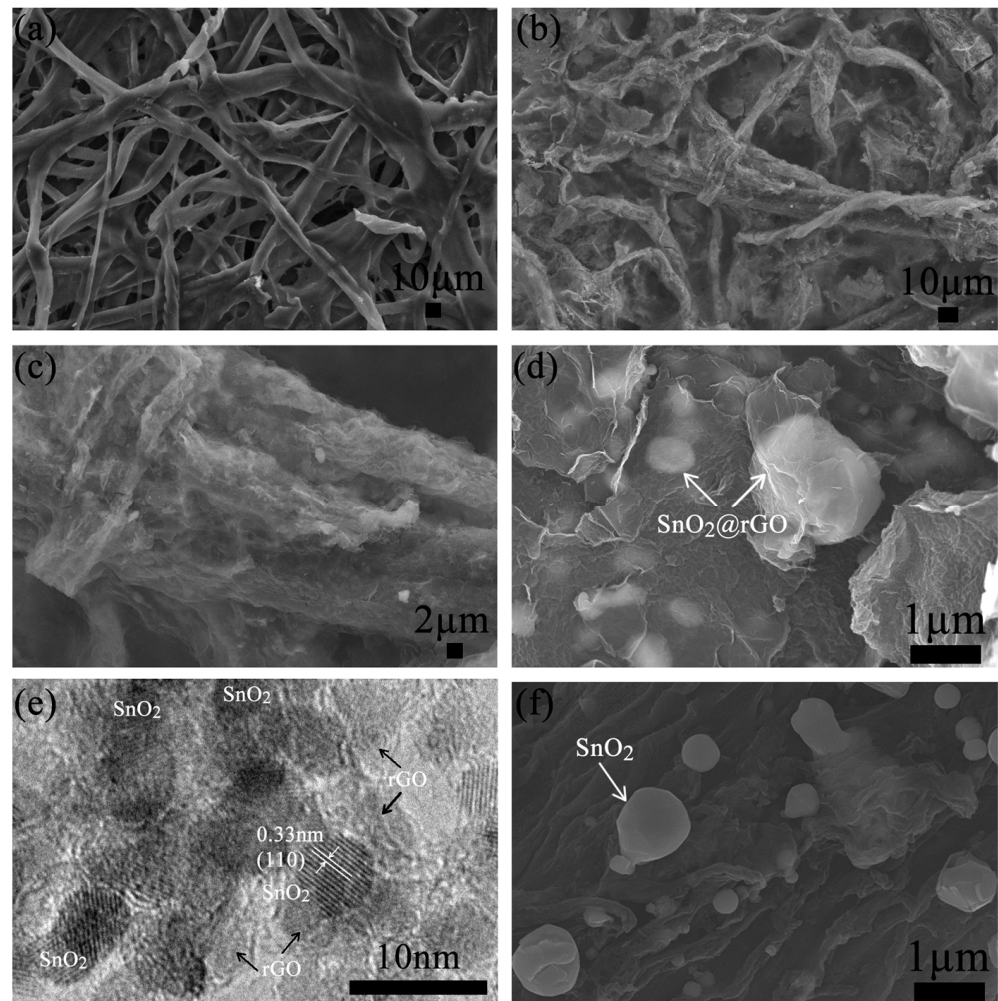


**Figure 4.** (**a**) SEM image of pure carbon fiber. (**b–d**) SEM image of flexible carbon fiber/$SnO_2$@rGO. (**e**) HRTEM image of flexible carbon fiber/$SnO_2$@rGO. (**f**) SEM image of carbon fiber/$SnO_2$.

The electrochemical performances of the samples as anodes for lithium-ion batteries (LIBs) were evaluated by cyclic voltammetry (CV), electrochemical impedance spectra (EIS), and galvanostatic charge-discharge (GCD). The flexible carbon fiber/$SnO_2$@rGO was directly used as the working electrodes without additives and binders. Figure 5a shows the CV curves of carbon fiber/$SnO_2$@rGO at a scan rate of 0.5 mV s$^{-1}$. In the first cathodic process, a peak around 0.5 V corresponds to the formation of a solid electrolyte interface (SEI) and the decomposition of $SnO_2$ to form Sn [51,52]. This peak disappears in the subsequent cycles to be replaced at a higher potential of 1.0 V, which corresponds to the reduction of $SnO_2$, i.e., $SnO_2 + 4\,Li^+ + 4e^- \rightarrow Sn + 2\,Li_2O$ [46]. The broad cathodic peak below 0.25 V is attributed to the formation of $Li_xSn$ alloys, i.e., $Sn + xLi^+ + xe^- \rightarrow Li_xSn$ ($0 \leq x \leq 4.4$), and the insertion of $Li^+$ into carbon and rGO [53,54]. In the anodic process, two

anodic peaks at 0.7 V and 1.3 V are observed. The peak at 0.7 V represents the dealloying of $Li_xSn$, i.e., $Li_xSn \rightarrow Sn + xLi^+ + xe^-$ ($0 \leq x \leq 4.4$) [46]. The peak at 1.3 V is due to the partial reversible oxidation of Sn into $SnO_2$, i.e., $Sn + 2Li_2O \rightarrow SnO_2 + 4Li^+ + 4e^-$ [7,54]. Figure 5b shows the discharge/charge curve of flexible carbon fiber/$SnO_2$@rGO at 50 mA g$^{-1}$. The initial discharge and charge capacities are 501.5 and 428 mAh g$^{-1}$, respectively, corresponding to an initial coulombic efficiency of 85.3%. The capacity drop in the first cycle can be attributed to the formation of SEI. The coulombic efficiency is above 94% in the subsequent three cycles at the current density of 50 mA g$^{-1}$.
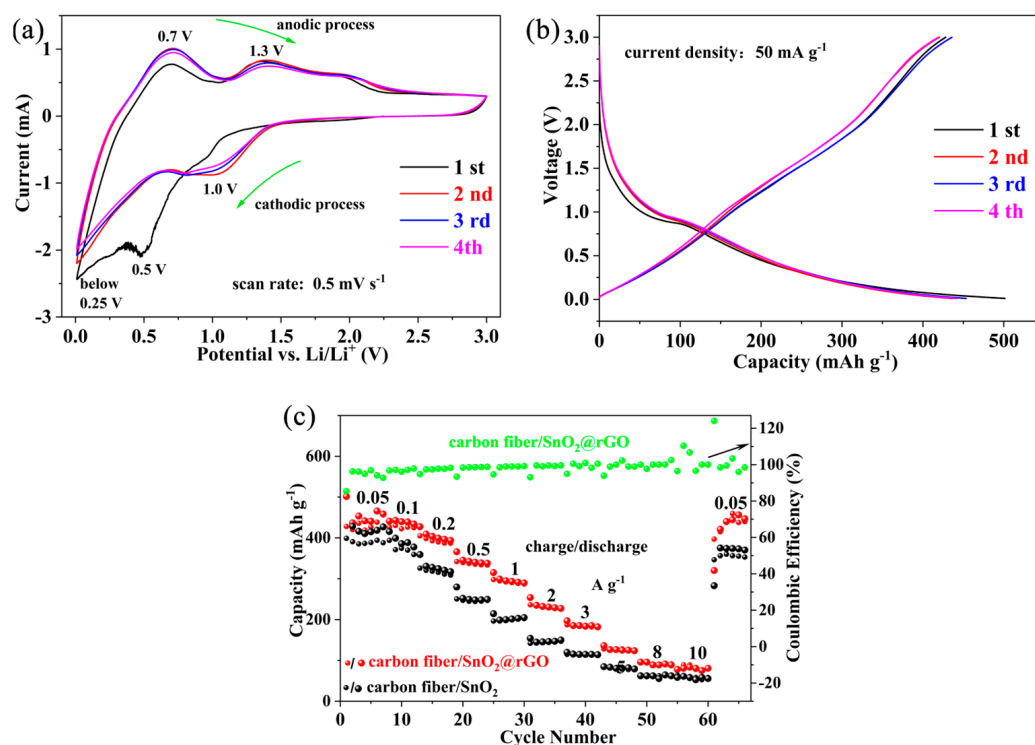


**Figure 5.** (**a**) CV curves and (**b**) discharge/charge curves of flexible carbon fiber/$SnO_2$@rGO for the initial four cycles, (**c**) rate capability.

Figure 5c shows the rate capabilities of flexible carbon fiber/$SnO_2$@rGO and carbon fiber/$SnO_2$. The flexible carbon fiber/$SnO_2$@rGO delivers outstanding capacities of 453, 393, 290, 234, 125, and 90 mAh g$^{-1}$ at 0.05, 0.2, 1, 2, 5, and 10 A g$^{-1}$, respectively, which significantly outperform that of carbon fiber/$SnO_2$. The higher capacity and better rate capability of carbon fiber/$SnO_2$@rGO can be attributed to the introduction of rGO and the formation of a sandwich-like structure. The introduced rGO sheets provide lithium storage sites and yield extra capacity. In addition, the structure of $SnO_2$ encapsulated by rGO overcomes the intrinsically poor electronic conductivity of $SnO_2$ and establishes a conductive network. These features facilitate rapid electrochemical reactions and enhance ion/electron transport kinetics. Additionally, the coulombic efficiency of carbon fiber/$SnO_2$@rGO remains above 92% since the second cycle at the current densities ranges from 50 mA g$^{-1}$ to 10 A g$^{-1}$ (Figure 5c).

The electrochemical kinetics of the electrodes were further investigated by EIS measures. An equivalent circuit model was applied to fit the EIS curves (Figure 6a), where $R_s$, $R_f$, and $R_{ct}$ represent the current collector and electrolyte resistance, the SEI layer resistance, and the charge transfer resistance. CPE1 and CPE2 represent the constant phase elements corresponding to the surface layer capacitor and the double layer capacitor. W represents the Warburg impedance associated with the Li$^+$ diffusion. The EIS curves reveal that the carbon fiber/$SnO_2$@rGO electrode exhibits a smaller semicircle diameter. The $R_f$ and $R_{ct}$ values of the carbon fiber/$SnO_2$@rGO electrode are lower than those of the carbon fiber/$SnO_2$ electrode (Table 1), indicating the lower resistance and faster charge transfer. To

gain further insight into Li$^+$ movement inside the electrodes, the Li$^+$ diffusion coefficient ($D_{Li+}$) was calculated by evaluating the Warburg coefficient ($\sigma$) from the low-frequency plot of Z' vs. $\omega^{-1/2}$ (Figure 6b) and using Equations (1) and (2) [55,56],

$$Z' = R_s + R_{ct} + \sigma\omega^{-1/2} \tag{1}$$

$$D_{Li+} = (R^2T^2)/(2A^2n^4F^4C^2\sigma^2) \tag{2}$$

where $\omega$ denotes the angular frequency, R is the gas constant, T is the absolute temperature, A is the electrode contact area, n is the number of transferred electrons, F is the Faraday constant, and C is the concentration of lithium ions. The value of $\sigma$ can be determined from the slope of the Z' vs. $\omega^{-1/2}$ plots (Figure 6b). The $D_{Li+}$ values of the carbon fiber/SnO$_2$@rGO electrode and the carbon fiber/SnO$_2$ electrode calculated from Equation (2) are $2.7 \times 10^{-14}$ cm$^2$ s$^{-1}$ and $2.2 \times 10^{-14}$ cm$^2$ s$^{-1}$, respectively. The larger $D_{Li+}$ of the carbon fiber/SnO$_2$@rGO electrode indicates faster Li$^+$ diffusion. These EIS results suggest that the sandwich-structured construction enhances the ion/electron transport kinetics. As a result, higher capacity and better rate capability are possible for carbon fiber/SnO$_2$@rGO electrodes.
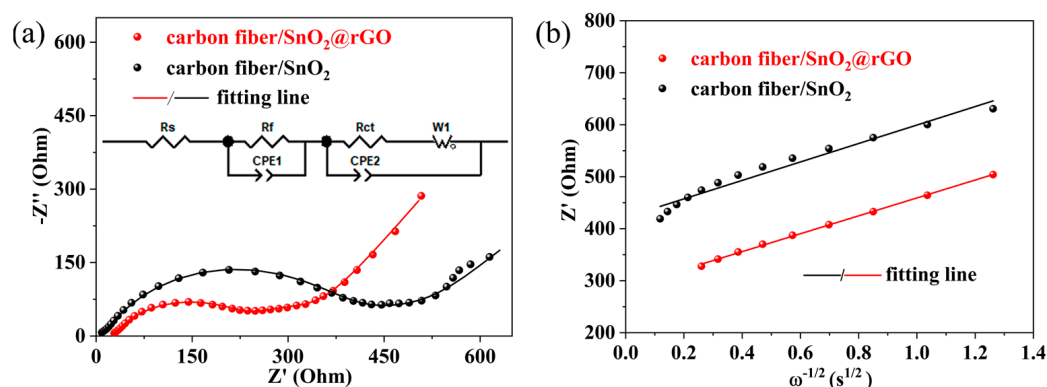


**Figure 6.** (**a**) EIS curves and the corresponding fitting plots of flexible carbon fiber/SnO$_2$@rGO and carbon fiber/SnO$_2$, with the inset showing the equivalent circuit used to fit the EIS curves. (**b**) Z' vs. $\omega^{-1/2}$ plots in the low-frequency range and the corresponding fitting plots.

**Table 1.** Relevant parameters of the samples simulated from the equivalent circuits.

| Sample | R$_f$ ($\Omega$) | R$_{ct}$ ($\Omega$) | $\sigma$ ($\Omega$ cm$^2$ s$^{-1/2}$) | D$_{Li+}$ (cm$^2$ s$^{-1}$) |
|---|---|---|---|---|
| carbon fiber/SnO$_2$@rGO | 228.6 | 100.9 | 172 | $2.7 \times 10^{-14}$ |
| carbon fiber/SnO$_2$ | 321.4 | 464 | 187.5 | $2.2 \times 10^{-14}$ |

Moreover, the carbon fiber/SnO$_2$@rGO electrode demonstrates excellent cycling stability. After 1000 cycles at 2 A g$^{-1}$, the capacity retention of carbon fiber/SnO$_2$@rGO electrode remains as high as 88% (Figure 7). In contrast, the carbon fiber/SnO$_2$ electrode experiences rapid capacity degradation in the initial stages, with a poor capacity retention of 13% after 300 cycles. Compared to the carbon fiber/SnO$_2$ electrode, the structure formed by rGO encapsulating SnO$_2$ helps mitigate the large volume expansion of SnO$_2$ particles and enhances the cycling stability of the carbon fiber/SnO$_2$@rGO electrode. Table 2 shows the performance comparison between this work and previous work in the literature. The carbon fiber/SnO$_2$@rGO electrode demonstrates outstanding cycling stability. The low capacity of the flexible carbon fiber/SnO$_2$@rGO electrode can be attributed to its heavier carbon fiber substrate. To achieve a flexible electrode, the carbon fiber/SnO$_2$@rGO electrode in this study was prepared at a lower carbonization temperature of 500 °C. This reduced temperature results in less decomposition of the filter paper, leading to the increased weight

of the carbon fiber substrate. The capacity reported in this study was calculated based on the total mass of the electrode. The heavier carbon fiber substrate consequently diminishes the overall capacity of the carbon fiber/$SnO_2$@rGO electrode.
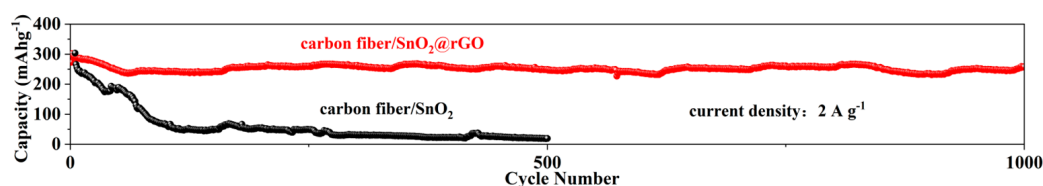


**Figure 7.** Cycling performance of flexible carbon fiber/$SnO_2$@rGO and carbon fiber/$SnO_2$.

**Table 2.** Electrochemical performance comparison for the $SnO_2$-based electrodes for LIBs.

| Electrodes | Capacity Retention | Rate Capability | References |
|---|---|---|---|
| **carbon fiber/$SnO_2$@rGO** | **88% (1000 cycles at 2 A g$^{-1}$)** | **453 mAh g$^{-1}$ (0.05 A g$^{-1}$);**<br>**393 mAh g$^{-1}$ (0.2 A g$^{-1}$);**<br>**290 mAh g$^{-1}$ (1 A g$^{-1}$);**<br>**234 mAh g$^{-1}$ (2 A g$^{-1}$);**<br>**125 mAh g$^{-1}$ (5 A g$^{-1}$)** | **this work** |
| $SnO_2$@graphene@graphene | 60% (120 cycles at 0.08 A g$^{-1}$) | 658.2 mAh g$^{-1}$ (0.16 A g$^{-1}$);<br>466.5 mAh g$^{-1}$ (0.4 A g$^{-1}$);<br>308.2 mAh g$^{-1}$ (0.8 A g$^{-1}$);<br>212.8 mAh g$^{-1}$ (4 A g$^{-1}$) | [57] |
| $SnO_2$/C | 84.5% (1000 cycles at 1 A g$^{-1}$) | 705 mAh g$^{-1}$ (0.2 A g$^{-1}$);<br>213 mAh g$^{-1}$ (5 A g$^{-1}$) | [58] |
| CGN/$SnO_2$-C | 71% (200 cycles at 0.1 A g$^{-1}$) | 686.5 mAh g$^{-1}$ (0.05 A g$^{-1}$);<br>361.1 mAh g$^{-1}$ (0.4 A g$^{-1}$);<br>270.2 mAh g$^{-1}$ (0.8 A g$^{-1}$) | [59] |
| $SnO_2$/CNT-GN | 87% (100 cycles at 0.2 A g$^{-1}$) | 1033 mAh g$^{-1}$ (0.5 A g$^{-1}$);<br>887 mAh g$^{-1}$ (2 A g$^{-1}$);<br>787 mAh g$^{-1}$ (5 A g$^{-1}$) | [60] |
| $SnO_2$@OSA-CNFs | 75% (100 cycles at 0.1 A g$^{-1}$) | 601 mAh g$^{-1}$ (0.5 A g$^{-1}$);<br>505 mAh g$^{-1}$ (1 A g$^{-1}$);<br>470 mAh g$^{-1}$ (2 A g$^{-1}$);<br>208 mAh g$^{-1}$ (5 A g$^{-1}$) | [45] |
| 3D $SnO_2$/graphene | 73.9% (50 cycles at 0.2 A g$^{-1}$) | 770.5 mAh g$^{-1}$ (0.2 A g$^{-1}$);<br>582.8 mAh g$^{-1}$ (1.5 A g$^{-1}$);<br>480.3 mAh g$^{-1}$ (3 A g$^{-1}$) | [61] |

## 4. Conclusions

Herein, a flexible carbon fiber/$SnO_2$@rGO electrode with a sandwich-like structure was prepared via adsorption assembly. This sandwich-structured construction effectively enhances ion/electron transport kinetics and mitigates the large volume expansion. These merits endow the carbon fiber/$SnO_2$@rGO electrode with high capacity, excellent rate capability, and superior cycle performance. In addition, the flexible carbon fiber/$SnO_2$@rGO electrode avoids the use of a current collector, a polymeric binder, and conductive additive, making it a promising anode for wearable and lightweight electronics applications.

**Data Availability Statement:** The original contributions presented in this study are included in the article. Further inquiries can be directed to the corresponding authors.

**Conflicts of Interest:** The authors declare no conflicts of interest.

## References

1. Li, H.; Wang, H.; Chan, D.; Xu, Z.; Wang, K.; Ge, M.; Zhang, Y.; Chen, S.; Tang, Y. Nature-inspired materials and designs for flexible lithium-ion batteries. *Carbon Energy* **2022**, *4*, 878–900. [CrossRef]

2. Zhang, W.; Shen, W.; Weng, Y.; Lv, R.; Kang, F.; Huang, Z.-H. Steam selective etching: A strategy to effectively enhance the flexibility and suppress the volume change of carbonized paper-supported electrodes. *ACS Nano* **2019**, *13*, 5731–5741. [CrossRef] [PubMed]

3. Han, D.Y.; Son, H.B.; Han, S.H.; Song, C.K.; Jung, J.; Lee, S.; Choi, S.S.; Song, W.J.; Park, S. Hierarchical 3D electrode design with high mass loading enabling high-energy-density flexible lithium-ion batteries. *Small* **2023**, *19*, 2305416. [CrossRef] [PubMed]

4. Xia, X.; Yang, J.; Liu, Y.; Zhang, J.; Shang, J.; Liu, B.; Li, S.; Li, W. Material choice and structure design of flexible battery electrode. *Adv. Sci.* **2023**, *10*, 2204875. [CrossRef] [PubMed]

5. Zhang, W.; Guo, Z.; Liang, Q.; Lv, R.; Shen, W.; Kang, F.; Weng, Y.; Huang, Z.-H. Flexible C-$Mo_2C$ fiber film with self-fused junctions as a long cyclability anode material for sodium-ion battery. *RSC Adv.* **2018**, *8*, 16657–16662. [CrossRef]

6. Zhang, W.; Pan, Z.-Z.; Lv, W.; Lv, R.; Shen, W.; Kang, F.; Yang, Q.-H.; Weng, Y.; Huang, Z.-H. Wasp nest-imitated assembly of elastic rGO/p-$Ti_3C_2T_x$ MXene-cellulose nanofibers for high-performance sodium-ion batteries. *Carbon* **2019**, *153*, 625–633. [CrossRef]

7. Min, X.; Sun, B.; Chen, S.; Fang, M.; Wu, X.; Liu, Y.g.; Abdelkader, A.; Huang, Z.; Liu, T.; Xi, K. A textile-based $SnO_2$ ultra-flexible electrode for lithium-ion batteries. *Energy Storage Mater.* **2019**, *16*, 597–606. [CrossRef]

8. Zhang, W.; Weng, Y.; Shen, W.; Lv, R.; Kang, F.; Huang, Z.-H. Scalable synthesis of lotus-seed-pod-like Si/$SiO_x$@CNF: Applications in freestanding electrode and flexible full lithium-ion batteries. *Carbon* **2020**, *158*, 163–171. [CrossRef]

9. Lauro, S.N.; Burrow, J.N.; Mullins, C.B. Restructuring the lithium-ion battery: A perspective on electrode architectures. *EScience* **2023**, *3*, 100152. [CrossRef]

10. Huang, A.; Ma, Y.; Peng, J.; Li, L.; Chou, S.-l.; Ramakrishna, S.; Peng, S. Tailoring the structure of silicon-based materials for lithium-ion batteries via electrospinning technology. *EScience* **2021**, *1*, 141–162. [CrossRef]

11. Wang, L.; He, Y.; Liu, D.; Liu, L.; Chen, H.; Hu, Q.; Liu, X.; Zhou, A. $SnO_2$ Quantum dots interspersed d-$Ti_3C_2T_x$ MXene heterostructure with enhanced performance for lithium ion battery. *J. Electrochem. Soc.* **2020**, *167*, 116522. [CrossRef]

12. Wang, L.; Wang, D.; Dong, Z.; Zhang, F.; Jin, J. Interface chemistry engineering for stable cycling of reduced GO/$SnO_2$ nanocomposites for lithium ion battery. *Nano Lett.* **2013**, *13*, 1711–1716. [CrossRef] [PubMed]

13. Shen, Z.; Guo, X.; Ding, H.; Yu, D.; Chen, Y.; Li, N.; Zhou, H.; Zhang, S.; Wu, J.; Pang, H. Construction of ternary Sn/$SnO_2$/nitrogen-doped carbon superstructures as anodes for advanced lithium-ion batteries. *Nano Res.* **2024**, *17*, 9721–9727. [CrossRef]

14. Lu, Z.; Kong, Z.; Jing, L.; Wang, T.; Liu, X.; Fu, A.; Guo, P.; Guo, Y.-G.; Li, H. Porous $SnO_2$/graphene composites as anode materials for lithium-ion batteries: Morphology control and performance improvement. *Energy & Fuels* **2020**, *34*, 13126–13136.

15. Jung, S.M.; Kim, D.W.; Jung, H.Y. Unconventional capacity increase kinetics of a chemically engineered $SnO_2$ aerogel anode for long-term stable lithium-ion batteries. *J. Mater. Chem. A* **2020**, *8*, 8244–8254. [CrossRef]

16. Cui, D.; Zheng, Z.; Peng, X.; Li, T.; Sun, T.; Yuan, L. Fluorine-doped $SnO_2$ nanoparticles anchored on reduced graphene oxide as a high-performance lithium ion battery anode. *J. Power Sources* **2017**, *362*, 20–26. [CrossRef]

17. Xie, W.; Gu, L.; Xia, F.; Liu, B.; Hou, X.; Wang, Q.; Liu, D.; He, D. Fabrication of voids-involved $SnO_2$@C nanofibers electrodes with highly reversible Sn/$SnO_2$ conversion and much enhanced coulombic efficiency for lithium-ion batteries. *J. Power Sources* **2016**, *327*, 21–28. [CrossRef]

18. Gao, C.; Jiang, Z.; Wang, P.; Jensen, L.R.; Zhang, Y.; Yue, Y. Optimized assembling of MOF/$SnO_2$/Graphene leads to superior anode for lithium ion batteries. *Nano Energy* **2020**, *74*, 104868. [CrossRef]

19. Hu, R.; Chen, D.; Waller, G.; Ouyang, Y.; Chen, Y.; Zhao, B.; Rainwater, B.; Yang, C.; Zhu, M.; Liu, M. Dramatically enhanced reversibility of $Li_2O$ in $SnO_2$-based electrodes: The effect of nanostructure on high initial reversible capacity. *Energ. Environ. Sci.* **2016**, *9*, 595–603. [CrossRef]

20. Gervillié, C.; Boisard, A.; Labbé, J.; Guérin, K.; Berthon-Fabry, S. Relationship between tin environment of $SnO_2$ nanoparticles and their electrochemical behaviour in a lithium ion battery. *Mater. Chem. Phys.* **2021**, *257*, 123461. [CrossRef]

21. Cheng, Y.; Wang, S.; Zhou, L.; Chang, L.; Liu, W.; Yin, D.; Yi, Z.; Wang, L. SnO$_2$ quantum dots: Rational design to achieve highly reversible conversion reaction and stable capacities for lithium and sodium storage. *Small* **2020**, *16*, 2000681. [CrossRef] [PubMed]

22. Zhu, W.; El-Khodary, S.A.; Li, S.; Zou, B.; Kang, R.; Li, G.; Ng, D.H.; Liu, X.; Qiu, J.; Zhao, Y. Roselle-like Zn$_2$Ti$_3$O$_8$/rGO nanocomposite as anode for lithium ion capacitor. *Chem. Eng. J.* **2020**, *385*, 123881. [CrossRef]

23. Wu, K.; Shi, B.; Qi, L.; Mi, Y.; Zhao, B.; Yang, C.; Wang, Q.; Tang, H.; Lu, J.; Liu, W. SnO$_2$ quantum dots@3D sulfur-doped reduced graphene oxides as active and durable anode for lithium ion batteries. *Electrochim. Acta* **2018**, *291*, 24–30. [CrossRef]

24. Liao, S.-Y.; Chen, J.; Cui, S.-F.; Shang, J.-Q.; Li, Y.-Z.; Cheng, W.-X.; Liu, Y.-D.; Cui, T.-T.; Shu, X.-G.; Min, Y.-G. CoS$_2$ enhanced SnO$_2$/rGO heterostructure quantum dots for advanced lithium-ion battery anode. *J. Power Sources* **2023**, *553*, 232265. [CrossRef]

25. Zhao, K.; Zhang, L.; Xia, R.; Dong, Y.; Xu, W.; Niu, C.; He, L.; Yan, M.; Qu, L.; Mai, L. SnO$_2$ Quantum dots@graphene oxide as a high-rate and long-life anode material for lithium-ion batteries. *small* **2016**, *12*, 588–594. [CrossRef]

26. Gao, L.; Wu, G.; Ma, J.; Jiang, T.; Chang, B.; Huang, Y.; Han, S. SnO$_2$ quantum dots@graphene framework as a high-performance flexible anode electrode for lithium-ion batteries. *ACS Appl. Mater. Interfaces* **2020**, *12*, 12982–12989. [CrossRef]

27. Cha, H.; Kim, J.; Lee, Y.; Cho, J.; Park, M. Issues and challenges facing flexible lithium-ion batteries for practical application. *Small* **2018**, *14*, 1702989. [CrossRef]

28. Fang, Z.; Wang, J.; Wu, H.; Li, Q.; Fan, S.; Wang, J. Progress and challenges of flexible lithium ion batteries. *J. Power Sources* **2020**, *454*, 227932. [CrossRef]

29. Qian, G.; Liao, X.; Zhu, Y.; Pan, F.; Chen, X.; Yang, Y. Designing flexible lithium-ion batteries by structural engineering. *ACS Energy Lett.* **2019**, *4*, 690–701. [CrossRef]

30. Liu, R.; Su, W.; He, P.; Shen, C.; Zhang, C.; Su, F.; Wang, C.-A. Synthesis of SnO$_2$/Sn hybrid hollow spheres as high performance anode materials for lithium ion battery. *J. Alloys Compd.* **2016**, *688*, 908–913. [CrossRef]

31. Li, Z.; Tan, Y.; Huang, X.; Zhang, W.; Gao, Y.; Tang, B. Three-dimensionally ordered macroporous SnO$_2$ as anode materials for lithium ion batteries. *Ceram. Int.* **2016**, *42*, 18887–18893. [CrossRef]

32. Gurunathan, P.; Ette, P.M.; Ramesha, K. Synthesis of hierarchically porous SnO$_2$ microspheres and performance evaluation as Li-ion battery anode by using different binders. *ACS Appl. Mater. Interfaces* **2014**, *6*, 16556–16564. [CrossRef] [PubMed]

33. Wei, W.; Du, P.; Liu, D.; Wang, H.; Liu, P. Facile mass production of nanoporous SnO$_2$ nanosheets as anode materials for high performance lithium-ion batteries. *J. Colloid Interf. Sci.* **2017**, *503*, 205–213. [CrossRef] [PubMed]

34. Liu, X.; Guo, J.; Liu, T.; Zhang, J.; Jia, Z.; Zhang, C. Mechanical simulation informed rational design of a soft-and-hard double-jacketed SnO$_2$ flexible electrode for high performance lithium-ion battery. *Energy Storage Mater.* **2021**, *35*, 520–529. [CrossRef]

35. Yanfeng, D.; Zongbin, Z.; Zhiyu, W.; Yang, L.; Xuzhen, W.; Jieshan, Q. Dually Fixed SnO$_2$ Nanoparticles on Graphene Nanosheets by Polyaniline Coating for Superior Lithium Storage. *ACS Appl. Mater. Interfaces* **2015**, *7*, 2444–2451.

36. Yuan, J.; Chen, C.; Hao, Y.; Zhang, X.; Zou, B.; Agrawal, R.; Wang, C.; Yu, H.; Zhu, X.; Yu, Y. SnO$_2$/polypyrrole hollow spheres with improved cycle stability as lithium-ion battery anodes. *J. Alloys Compd.* **2017**, *691*, 34–39. [CrossRef]

37. Li, B.; Bi, R.; Yang, M.; Gao, W.; Wang, J. Coating conductive polypyrrole layers on multiple shells of hierarchical SnO$_2$ spheres and their enhanced cycling stability as lithium-ion battery anode. *Appl. Surf. Sci.* **2022**, *586*, 152836. [CrossRef]

38. Yi, L.; Liu, L.; Guo, G.; Chen, X.; Zhang, Y.; Yu, S.; Wang, X. Expanded graphite@SnO$_2$@polyaniline composite with enhanced performance as anode materials for lithium ion batteries. *Electrochim. Acta* **2017**, *240*, 63–71. [CrossRef]

39. Ming, L.; Zhang, B.; Zhang, J.-F.; Wang, X.-W.; Li, H.; Wang, C.-H. SnO$_2$@C/expanded graphite nanosheets as high performance anode materials for lithium ion batteries. *J. Alloys Compd.* **2018**, *752*, 93–98. [CrossRef]

40. Lu, X.; Chen, Y.; Tian, Q.; Zhang, W.; Sui, Z.; Chen, J. Enabling improved cycling stability of hollow SnO$_2$/C composite anode for lithium-ion battery by constructing a built-in porous carbon support. *Appl. Surf. Sci.* **2021**, *537*, 148052. [CrossRef]

41. Cao, B.; Liu, Z.; Xu, C.; Huang, J.; Fang, H.; Chen, Y. High-rate-induced capacity evolution of mesoporous C@SnO$_2$@C hollow nanospheres for ultra-long cycle lithium-ion batteries. *J. Power Sources* **2019**, *414*, 233–241. [CrossRef]

42. Liang, J.; Yu, X.Y.; Zhou, H.; Wu, H.B.; Ding, S.; Lou, X.W. Bowl-like SnO$_2$@carbon hollow particles as an advanced anode material for lithium-ion batteries. *Angew. Chem.* **2014**, *126*, 13017–13021. [CrossRef]

43. Bonino, C.A.; Ji, L.; Lin, Z.; Toprakci, O.; Zhang, X.; Khan, S.A. Electrospun carbon-tin oxide composite nanofibers for use as lithium ion battery anodes. *ACS Appl. Mater. Interfaces* **2011**, *3*, 2534–2542. [CrossRef] [PubMed]

44. Li, H.; Yang, L.; Liu, J.; Li, S.; Fang, L.; Lu, Y.; Yang, H.; Liu, S.; Lei, M. Improved electrochemical performance of yolk-shell structured SnO$_2$@void@C porous nanowires as anode for lithium and sodium batteries. *J. Power Sources* **2016**, *324*, 780–787. [CrossRef]

45. Wang, X.; Sun, N.; Dong, X.; Huang, H.; Qi, M. Electrospun layers by layers orderly stacked SnO$_2$@ aligned carbon nanofibers as high conductivity, long cycle life self-standing anode for reversible lithium ions batteries. *Surf. Interfaces* **2022**, *29*, 101814. [CrossRef]

46. Yang, L.; Dai, T.; Wang, Y.; Xie, D.; Narayan, R.L.; Li, J.; Ning, X. Chestnut-like SnO$_2$/C nanocomposites with enhanced lithium ion storage properties. *Nano Energy* **2016**, *30*, 885–891. [CrossRef]

47. Habibi, A.; Mousavi, M.R.; Yasoubi, M.; Sanaee, Z.; Ghasemi, S. Plasma-enhanced chemical vapor deposition for fabrication of yolk-shell SnO$_2$@ Void@ C nanowires, as an efficient carbon coating technique for improving lithium-ion battery performance. *Mat. Sci. Semicon. Proc.* **2022**, *149*, 106901. [CrossRef]

48. Han, S.; Pu, X.; Li, X.; Liu, M.; Li, M.; Feng, N.; Dou, S.; Hu, W. High areal capacity of Li-S batteries enabled by freestanding CNF/rGO electrode with high loading of lithium polysulfide. *Electrochim. Acta* **2017**, *241*, 406–413. [CrossRef]

49. Li, J.; Zhang, H.; Luo, L.; Li, H.; He, J.; Zu, H.; Liu, L.; Liu, H.; Wang, F.; Song, J. Blocking polysulfides with a Janus Fe₃C/N-CNF@RGO electrode via physiochemical confinement and catalytic conversion for high-performance lithium-sulfur batteries. 1 **2021**, *9*, 2205–2213. [CrossRef]

50. Li, X.; Meng, X.; Liu, J.; Geng, D.; Zhang, Y.; Banis, M.N.; Li, Y.; Yang, J.; Li, R.; Sun, X. Tin oxide with controlled morphology and crystallinity by atomic layer deposition onto graphene nanosheets for enhanced lithium storage. *Adv. Funct. Mater.* **2012**, *22*, 1647–1654. [CrossRef]

51. Lin, J.; Peng, Z.; Xiang, C.; Ruan, G.; Yan, Z.; Natelson, D.; Tour, J.M. Graphene nanoribbon and nanostructured SnO₂ composite anodes for lithium ion batteries. *ACS Nano* **2013**, *7*, 6001–6006. [CrossRef] [PubMed]

52. Di Lupo, F.; Gerbaldi, C.; Meligrana, G.; Bodoardo, S.; Penazzi, N. Novel SnO₂/mesoporous carbon spheres composite anode for Li-ion batteries. *Int. J. Electrochem. Sc.* **2011**, *6*, 3580–3593. [CrossRef]

53. Li, Y.; Zhang, H.; Shen, P.K. Ultrasmall metal oxide nanoparticles anchored on three-dimensional hierarchical porous gaphene-like networks as anode for high-performance lithium ion batteries. *Nano Energy* **2015**, *13*, 563–572. [CrossRef]

54. Liu, Q.; Dou, Y.; Ruan, B.; Sun, Z.; Chou, S.L.; Dou, S.X. Carbon-coated hierarchical SnO₂ hollow spheres for lithium ion batteries. *Chem-Eur. J.* **2016**, *22*, 5853–5857. [CrossRef] [PubMed]

55. Cheng, Y.; Huang, J.; Li, J.; Xu, Z.; Cao, L.; Ouyang, H.; Yan, J.; Qi, H. SnO₂/super P nanocomposites as anode materials for Na-ion batteries with enhanced electrochemical performance. *J. Alloys Compd.* **2016**, *658*, 234–240. [CrossRef]

56. Saikia, D.; Deka, J.R.; Chou, C.-J.; Kao, H.-M.; Yang, Y.-C. 3D interpenetrating cubic mesoporous carbon supported nanosized SnO₂ as an efficient anode for high performance lithium-ion batteries. *J. Alloys Compd.* **2019**, *791*, 892–904. [CrossRef]

57. Zhu, J.; Zhang, G.; Yu, X.; Li, Q.; Lu, B.; Xu, Z. Graphene double protection strategy to improve the SnO₂ electrode performance anodes for lithium-ion batteries. *Nano Energy* **2014**, *3*, 80–87. [CrossRef]

58. Li, L.; Zhang, H.; Li, Z.; Zhong, W.; Liao, H.; Li, Z. Rapid preparation of SnO₂/C nanospheres by using organotin as building blocks and their application in lithium-ion batteries. *RSC Adv.* **2017**, *7*, 34442–34447. [CrossRef]

59. Zhang, X.; Huang, X.; Zhang, X.; Xia, L.; Zhong, B.; Zhang, T.; Wen, G. Cotton/rGO/carbon-coated SnO₂ nanoparticle-composites as superior anode for Lithium ion battery. *Mater. Design* **2017**, *114*, 234–242. [CrossRef]

60. Wang, M.-S.; Wang, Z.-Q.; Yang, Z.-L.; Huang, Y.; Zheng, J.; Li, X. Carbon nanotube-graphene nanosheet conductive framework supported SnO₂ aerogel as a high performance anode for lithium ion battery. *Electrochim. Acta* **2017**, *240*, 7–15. [CrossRef]

61. Tian, R.; Zhang, Y.; Chen, Z.; Duan, H.; Xu, B.; Guo, Y.; Kang, H.; Li, H.; Liu, H. The effect of annealing on a 3D SnO₂/graphene foam as an advanced lithium-ion battery anode. *Sci. Rep.* **2016**, *6*, 19195. [CrossRef] [PubMed]